Highly loaded well dispersed stable Ni species in $Ni_X Mg_2 AlO_Y$ nanocomposites: Application to hydrogen production from bioethanol

Wenhao Fang [a,b], Sébastien Paul [a,b,c], Mickaël Capron [a,b], Ankush V. Biradar [d], Shubhangi B. Umbarkar [d], Mohan K. Dongare [d], Franck Dumeignil [a,b,e], Louise Jalowiecki-Duhamel [a,b,*]

[a] Université Lille Nord de France, 59000 Lille, France
[b] Centre National de la Recherche Scientifique UMR8181, Unité de Catalyse et Chimie du Solide, UCCS, 59655 Villeneuve d'Ascq, France
[c] Ecole Centrale de Lille, 59655 Villeneuve d'Ascq, France
[d] CSIR-National Chemical Laboratory, Catalysis Division, 411008 Pune, India
[e] Institut Universitaire de France, Maison des Universités, 103 Boulevard Saint-Michel, 75005 Paris, France

ABSTRACT

Inexpensive $Ni_X Mg_2 AlO_Y$ nanocomposites with high Ni content (Ni wt% > 40%) are developed as efficient catalysts for the sustainable hydrogen production from a mixture of ethanol and water at low temperature. The $Ni_X Mg_2 AlO_Y$ nanocomposites are composed of small and uniform nanoparticles (4–6 nm) of NiO, Ni–Mg–(Al)–O and/or MgO. The strong interactions existing between Ni^{2+} cations and Mg^{2+} and/or Al^{3+} cations either in the Ni–Mg–(Al)–O solid solution and/or at the interface of nanoparticles of NiO and/or Ni–Mg–(Al)–O make the catalyst highly active and stable. The behavior of the solids is analyzed in the presence of low and high concentrations of ethanol while maintaining a H_2O/EtOH molar ratio of 3. The $Ni_X Mg_2 AlO_Y$ catalysts are shown to be efficient toward H_2 production between 250 and 650 °C. In the presence of low concentration of ethanol, on the highly loaded Ni compound ($Ni_{12} Mg_2 AlO_Y$), total conversion of ethanol is obtained at 250 °C without formation of CO and carbon, and at 300 °C a H_2 yield of $3\ mol\ mol_{EtOH}{}^{-1}$ is obtained without the formation of CO, exhibiting a remarkable stability with the time on stream even if some carbon is formed. In high concentration of ethanol, total conversion of ethanol is obtained at 450 °C on the highly loaded Ni compound ($Ni_{12} Mg_2 AlO_Y$). In such conditions, a stable co-generation of carbon nanofibrous materials which amount increases with Ni content is also obtained. The catalytic stability is related to the type and morphology of the carbon species formed. The correlations among the catalyst properties, the catalytic performances and the characterizations are thoroughly discussed.

© 2014 Elsevier B.V. All rights reserved.

1. Introduction

Hydrogen (H_2) and its diversity of applications are critical to any clean energy economy. At the international level, hydrogen is viewed as a major vector that could contribute to the reduction of the global dependence upon fossil fuels and to the lowering of the greenhouse-gas emission and atmospheric pollution [1]. In the point view of environmentally friendly and sustainable energy development strategy, H_2 production by transformation of renewable sources, such as biomass or biomass-derived materials, is proposed to be an alternatively desirable route [2–4].

Bioethanol is one of the most important platform molecules as the chemical carrier of hydrogen and it is currently produced from biomass or agricultural wastes by the mature fermentation technology. Thus, ethanol steam reforming (ESR) is a very ideal route to produce hydrogen [Eq. (1)] [5–10]. Moreover, ESR could support a carbon-free emission in theory since the CO_2 produced can be recycled back during biomass growth. However, the endothermic ESR requires energy input, which leads to the high operation costs and to the inconvenience for the onboard and stationary application of hydrogen, i.e. fuel cells. In such a context, it is today a major target to develop inexpensive catalysts that are active at low temperature, selective, and stable to address the challenges of ESR [11–13]. One is supposed to design the catalyst that is able to optimize the

balance of ESR and WGS (water gas shift) to obtain the high activity and high H_2 yield at low temperature.

$$C_2H_5OH + 3H_2O \rightarrow 6H_2 + 2CO_2, \quad \Delta H^0_{298\,K} = +174\,kJ\,mol^{-1} \quad (1)$$
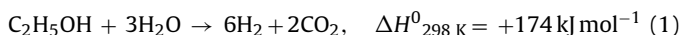
It is known that metal–support interaction plays an important role during the preparation step and thermal treatments, since both of them can define the properties of final catalysts: reducibility, resistance to thermal sintering of the active sites or metallic dispersion. The reducibility, the catalytic activities and coking resistant behaviors of catalysts are affected by their surface and structural properties, so the methodology used in the preparation can lead to the obtainment of materials with important properties for applications in catalytic processes. It is well known that the morphology and structure are strongly affected by the synthesis method, metal precursor, and/or support materials. Since particle size and agglomeration of a metal usually increase with its loading onto the supports, the synthesis procedure of a highly loaded Ni catalyst with a narrow size distribution remains a great challenge. As a matter of fact, the preparation of stable nanoparticles in high proportion has huge applications not only in catalysis [14,15].

In the recent literature, only a few systems have been reported as good candidates for high-yield H_2 production from ESR at low temperatures (< 400 °C). Ciambelli et al. [16] investigated the support effect on Pt catalysts and reported Pt/CeO_2 as active catalyst for ESR with complete ethanol conversion at 300 °C. Chen et al. [17] found that Fe-promoted $Rh/Ca–Al_2O_3$ catalyst can lead to a high H_2 yield and a long Rh life span between 350 and 400 °C. In another study, a bimetallic $Rh–Co/CeO_2$ catalyst was reported to show a high H_2 yield at 300 °C, but deactivation occurred attributed to both metal oxidation and carbon deposition [18]. Although the noble metal catalysts exhibit good performances for ESR, the high price and low availability would eventually limit the future application. Even if Ni-based catalysts often suffer deactivation due to the carbon deposition, Ni-based catalysts are very attractive and extensively studied owing to their fairly good activity in the cleavage of the C–C and C–H bonds [19–24].

Besides, carbon can exist in different forms among which carbon nanomaterials are considered as the strategic materials for nanotechnology [25]. Carbon nanotubes (CNTs) and carbon nanofibers (CNFs) have attracted worldwide attention due to their extraordinary mechanical, electric, and catalytic properties [26–29]. Thereby, the synthesis of carbon nanofibrous materials with high quality and quantity at low cost is of great importance [25,30]. Pressures of an evolving sustainable society are calling for awareness upon chemistry science and of a need to develop technology leading to energy and materials by utilizing benign, resource efficient, and environmentally sound methodologies. It has been shown that the chemical catalytic transformation of biomass materials is an alternative way to produce hydrogen and CNTs. In the literature, multi-walled CNTs from ethanol decomposition (in the absence of water) have been reported, and the influences of temperature, metal loading, and feeding rate on carbon growth were studied [31–34]. A concept study was dedicated to the co-production of H_2 and multi-walled CNTs from ethanol decomposition at high temperatures (500–900 °C). Fe- and Ni-based catalysts were mainly reported, such as Fe/Al_2O_3, Ni/Al_2O_3, $LaNiO_3$, and $LaFeO_3$ [31–34]. Compared to ethanol decomposition, working in the presence of water allows the use of bioethanol and avoids some of the costly steps involved in the purification. Recently, it was reported that hydrogen together with high-quality CNTs can be generated from glycerol reforming in the presence of water over Ni–Mg–Al catalyst at temperature higher than 600 °C, allowing increasing the economic and environmental value of reforming process of bio-based hydrocarbon [35]. If the catalytic system can remain stable even in the presence of production of carbon nanomaterials, such ESR process not only allows producing

H_2, eliminating CO_2 emission and helping to clean the planet, but also bringing an added bonus. To our knowledge, there are only few publications on the high H_2 production accompanied with the production of CNTs or CNFs from ethanol steam reforming. We reported Ce–Ni mixed oxides as efficient catalysts for H_2 production from ESR between 450 and 650 °C over which carbon nanofibrous materials formation has been shown [36]. And more recently, we reported $Ni_XMg_2AlO_Y$ ($0 < X \leq 4$) ex-hydrotalcite catalysts for the catalytic transformation of ethanol in the presence of water to hydrogen [37].

Herein we report very active, stable, and inexpensive $Ni_XMg_2AlO_Y$ catalysts with well-dispersed highly loaded Ni species (40–60 Ni wt%) that are applied to the catalytic transformation at low temperature of bioethanol (mixture of ethanol and water) to hydrogen and when varying ethanol concentration to hydrogen and carbon nanofibrous materials. Different parameters are analyzed, such as reaction temperature, Ni content, and concentration of ethanol and their influences on catalytic stability are studied. Besides, the $Ni_XMg_2AlO_Y$ catalysts (before and after reaction) are characterized by various physicochemical techniques. Carbonaceous species formed are also systematically characterized to identify their type and morphology. Furthermore, the correlations between the catalyst properties and the catalytic performances are fully discussed, allowing us to participate to the open debate on this interesting catalytic process and propose an active site and a possible mechanism.

2. Experimental

2.1. Catalyst preparation

$Ni_XMg_2AlO_Y$ nanocomposite catalysts were obtained by thermal treatment of the Ni_XMg_2Al HT-like precursors at 500 °C in air. The catalyst precursors were prepared by the co-precipitation method using $NaOH/Na_2CO_3$ as precipitant. An aqueous mixture solution (1 M) of nitrate metals with a molar ratio of Ni/Mg/Al = X/2/1 was added drop-wise into NaOH (1 M) and Na_2CO_3 (0.5 M) mixed solution at room temperature. And then the slurry was kept vigorous stirring at 80 °C for 18 h. Afterwards the solids were recovered by filtration and were washed by excesive deinionized water. Finally, the precursors were oven dried at 120 °C overnight.

2.2. Catalytic performance

The catalytic reaction was performed under the atmospheric pressure in a fixed-bed quartz flow reactor (inner diameter: 8 mm). Heating of the reactor was provided by a programmable oven. The catalyst (50 mg) was previously in situ treated in H_2 at 450 °C for 10 h. The reactant mixture of water–ethanol (molar ratio: $H_2O/EtOH = 3$) was injected into a heating chamber by HPLC pump, and then the vaporized steam was fed into the reactor using N_2 as carrier with a flow rate of 60 mL min^{-1}. The feed and product outlet gases were analyzed online by gas chromatography (TRACE GC ULTRA) equipped with a thermal-conductivity detector (TCD) and the flame ionization detector (FID).

In order to analyze the influence of the concentration of ethanol, different liquid flows of the ethanol–water mixture were used while the $H_2O/EtOH$ molar ratio was always kept constant at 3. The liquid flows were 0.100, 0.010, and 0.005 mL min^{-1} corresponding to theoretical vapor flow of 80, 8, and 4 mL min^{-1}, respectively. To allow easy comparison with the literature, 0.100 mL min^{-1} of liquid flow corresponds to 33.3 vol.% of ethanol. The concentration of ethanol in mol.% has been analyzed by GC, and the liquid flows of 0.100, 0.010, and 0.005 mL min^{-1} lead to 14 (concentrated conditions), 3, and 1 mol.% of ethanol, respectively.

Catalytic performances were reported after at least 5 h of the reaction by ethanol conversion (X_{EtOH}), products molar composition (C_i), and H_2 yield (Y_{H2}), based on the following equations [Eqs. (2)–(4)] where a yield of 6 is in theory equivalent to 100% [Eq. (1)]:

$$X_{EtOH} = \frac{n_{EtOH,in} - n_{EtOH,out}}{n_{EtOH,in}} \times 100\% \tag{2}$$

$$C_i = \frac{n_i}{\sum_{products} n_i} \times 100\% \tag{3}$$

$$Y_{H_2} = \frac{n_{H_2}}{n_{EtOH,in} X_{EtOH}} \leq 6 \tag{4}$$

2.3. Catalyst characterizations

The metal loadings were analyzed by ICP-MS technique from CNRS-Service Central d'Analyses and the Ni/Mg/Al molar ratio was then deduced.

The BET surface area was measured by N_2 physisorption at −196 °C by using a Micromeritics TriStar II 3020 Surface-Area and Porosimetry analyzer. The sample was previously out-gassed under vacuum at 150 °C for 3 h.

XRD was carried out with a Bruker D8 Advance X-ray diffractometer equipped with a fast detector type LynxEye with a copper anticathode. The patterns were registered in the 2θ domain (10–90°) with a measured step of 0.02°, and the time integration was fixed to 0.3 s. The crystallite size was calculated by using the Scherrer equation.

In situ XRD in H_2 was performed on a Bruker D8 Advance type HT1200N X-ray diffractometer equipped with a fast detector type VANTEC with a copper anticathode. A mixed gas of 3 vol.% H_2–97 vol.% Ar was employed with a heating rate of 10 °C min^{-1} from room temperature to 650 °C.

XPS analysis was performed on a Thermo VG Escalab 220 XL spectrometer under ultrahigh vacuum, using a twin Al X-ray source (1486.6 eV) at a pass energy of 40 eV. The solids in the form of pellets were fixed on a copper holder with copper tape. The charge effect was adjusted by reference to the C 1s peak at 285 eV for all the samples before the reaction. While for the catalysts after the reaction, a reference to Al 2p peak at 74.7 eV was taken into account.

H_2-TPR was performed on a Micromeritics Autochem II Chemisorption analyzer, and the H_2 consumption was measured by a TCD detector. The sample was treated in the 5 vol.% H_2–95 vol.% Ar mixtures with a flow rate of 30 mL min^{-1}. The temperature was increased to 1000 °C at a heating rate of 10 °C min^{-1}.

2.4. Carbon characterizations

The amount of solid carbon formed was determined by measuring the mass variation of the catalyst after test. The production of carbon was reported in gram of carbon produced per gram of catalyst per hour taking into account the duration of the catalytic test. The carbon for characterization is manually separated from the used catalysts without any treatment or purification.

O_2-TPO was performed on a Micromeritics Autochem 2920 analyzer. The sample was treated in the 5 vol.% O_2–95 vol.% He mixtures with a flow rate of 50 mL min^{-1}. The temperature was increased to 1000 °C at a heating rate of 5 °C min^{-1}. The desorption species from the sample were detected by using a OmniStar GSD 300 O mass spectrometer.

Raman spectra of carbonaceous species were acquired on a Labram Infinity HORIBA JOBIN YVON Raman spectrometer using a visible laser with a wavelength of λ = 532 nm at room temperature.

TEM images were obtained by a FEI Tecnai G2 20 transmission electron microscope at an acceleration voltage of 200 kV. The sample was previously ultrasonically dispersed in acetone and then

drops of the suspension were applied onto a copper grid-supported transparent carbon film.

3. Results and discussion

3.1. Production of H_2 and distribution of gas-phase products

Ethanol steam reforming was studied in the present work over the $Ni_3Mg_2AlO_Y$ and $Ni_{12}Mg_2AlO_Y$ catalysts. Different parameters were investigated, including reaction temperature, Ni content, concentration of ethanol vapor, and their influences on the catalytic stability.

To analyze the behavior of the catalysts in harsh conditions, ESR was first studied as a function of the reaction temperature in concentrated conditions of ethanol (EtOH/H_2O/N_2 = 14/42/44). Fig. 1 reports the results obtained at the steady state after 5 h of reaction at each temperature. The $Ni_3Mg_2AlO_Y$ and $Ni_{12}Mg_2AlO_Y$ catalysts demonstrate relatively similar evolution for ethanol conversion and products distribution. However, on the $Ni_{12}Mg_2AlO_Y$ catalyst, a higher conversion is observed; about 40% ethanol
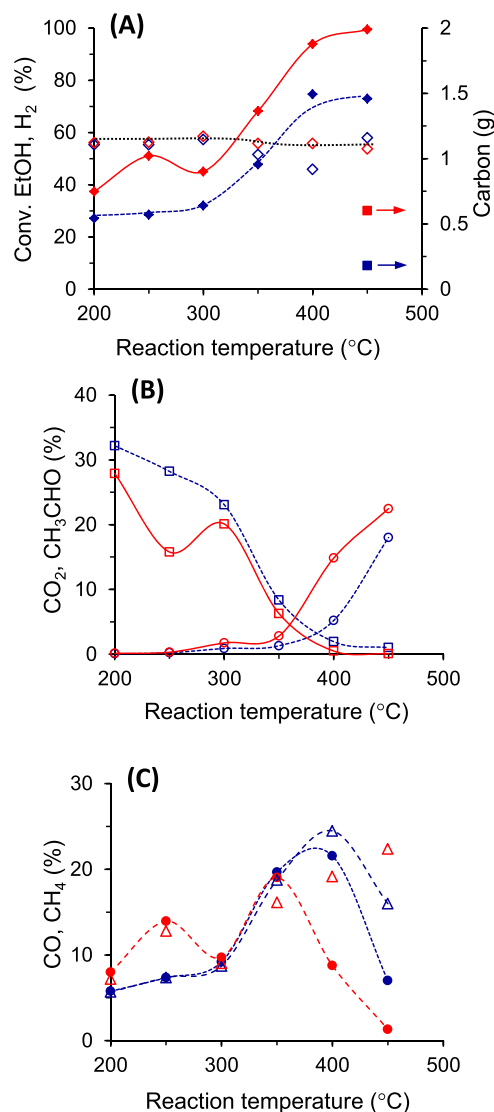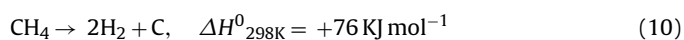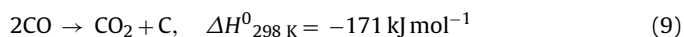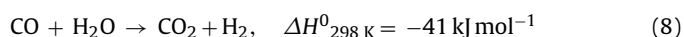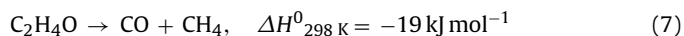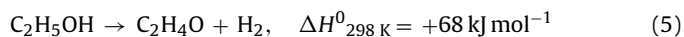

Fig. 1. Conversion of ethanol (♦), gas-phase products distribution: H_2 (◇), CO_2 (○), CH_3CHO (□), CO (●), CH_4 (△), and carbon formation (■) on the $Ni_3Mg_2AlO_Y$ (blue) and $Ni_{12}Mg_2AlO_Y$ (red) catalysts as a function of the reaction temperature. EtOH/H_2O/N_2 = 14/42/44. Each point is reported after 5 h of reaction, except carbon measured after test.

conversion is already obtained at very low temperature of 200 °C. As expected, conversion undergoes a global increase with reaction temperature, and it approaches to 100% at 400 °C, showing good activity for ESR at low temperature. Ethanol conversion is ameliorated compared with the recent values reported on Ni–Mg–Al catalysts, where the $Ni_{0.5}Mg_{2.5}Al$ catalyst gave total ethanol conversion at 450 °C in the presence of 9 mol.% of ethanol [38]. As a matter of fact, increasing Ni content allows increasing ethanol conversion [37]. In another study, the $Ni_{50}MgAl$ catalyst exhibited activity lower than 30% when the reaction temperature is below 450 °C working with 9.2 mol.% of ethanol [39]. It is important to recall that the high conversion of ethanol that is injected in high concentration leads to a high production of gases, and H_2 formation relative to all the gas phase products (dry basis) maintains about 55% (in mol.%). The other products obtained in gas-phase are acetaldehyde, CO_2, CO, and CH_4 (Fig. 1). Acetaldehyde shows a decline when reaction temperature increases, and it finally eliminates at 400 °C. Only trace of CO_2 is analyzed at temperature lower than 300 °C. CO_2 starts to rise from 350 °C and rapidly reaches about 20% at 450 °C. CH_4 globally increases with reaction temperature up to about 400 °C; while CO presents a maximum at about 20% between 350 and 400 °C, afterwards it decreases.

It seems that dehydrogenation and decomposition of ethanol are the main reactions when the temperature is lower than 400 °C. In fact, there is no C_2H_4 formed whatever the temperature. It was disclosed that ethanol is more feasible to dehydrogenate to form acetaldehyde and H_2 [Eq. (5)] over the basic oxides [6], e.g. $MgAl_2O_4$. It was reported that ethanol could probably decompose to CO, CH_4, and H_2 [Eq. (6)] over the catalyst possessing the high activity in the rupture of C–C bond, e.g. Ni-based catalyst [10,23]. Acetaldehyde can further decompose to CO and CH_4 [Eq. (7)]. When reaction temperature is higher than 400 °C, ESR starts to become the main reaction. It is known that high temperature facilitates ESR, while CO transformation by WGS [Eq. (8)] is favored at low temperature. In the temperature range investigated, the $Ni_{12}Mg_2AlO_Y$ catalyst leads to relatively higher ethanol conversion and CO_2 formation, showing the influence of Ni content. In addition, the decrease of CO is advanced on the $Ni_{12}Mg_2AlO_Y$ catalyst. It is certainly due to the carbon formation by the disproportionation of CO [Eq. (9)] [40]. This is in agreement with the higher quantity of carbon formation on the $Ni_{12}Mg_2AlO_Y$ catalyst, as reported in Fig. 1. A carbon formation of 0.6 g is obtained on $Ni_{12}Mg_2AlO_Y$ catalyst after the overall reaction (200–450 °C), while 0.18 g of carbon is obtained on $Ni_3Mg_2AlO_Y$ catalyst. Carbon can also be obtained from methane [Eq. (10)], however, methane does not decrease on the $Ni_{12}Mg_2AlO_Y$ catalyst up to 450 °C in such conditions.

$$C_2H_5OH \rightarrow C_2H_4O + H_2, \quad \Delta H^0_{298\,K} = +68\,kJ\,mol^{-1} \tag{5}$$

$$C_2H_5OH \rightarrow CO + CH_4 + H_2, \quad \Delta H^0_{298\,K} = +49\,kJ\,mol^{-1} \tag{6}$$

$$C_2H_4O \rightarrow CO + CH_4, \quad \Delta H^0_{298\,K} = -19\,kJ\,mol^{-1} \tag{7}$$

$$CO + H_2O \rightarrow CO_2 + H_2, \quad \Delta H^0_{298\,K} = -41\,kJ\,mol^{-1} \tag{8}$$

$$2CO \rightarrow CO_2 + C, \quad \Delta H^0_{298\,K} = -171\,kJ\,mol^{-1} \tag{9}$$

$$CH_4 \rightarrow 2H_2 + C, \quad \Delta H^0_{298K} = +76\,KJ\,mol^{-1} \tag{10}$$

The efficiency of the $Ni_{12}Mg_2AlO_Y$ catalyst toward H_2 production is clearly seen in Fig. 2 by using diluted conditions in ethanol (EtOH/H_2O/N_2 = 1/3/96) in order to avoid any problem due to the volume variation when a big amount of reactant vapor is introduced. It has to be noticed that the results reported in Fig. 2 have been obtained in continuity for each ethanol concentration, but stopped and started again with fresh catalyst (new catalyst after H_2 treatment at 450 °C) when changing ethanol concentration. Complete ethanol conversion is achieved at temperatures as low as 250 and 300 °C. Only H_2, CO_2, and CH_4 are formed in the gas phase.
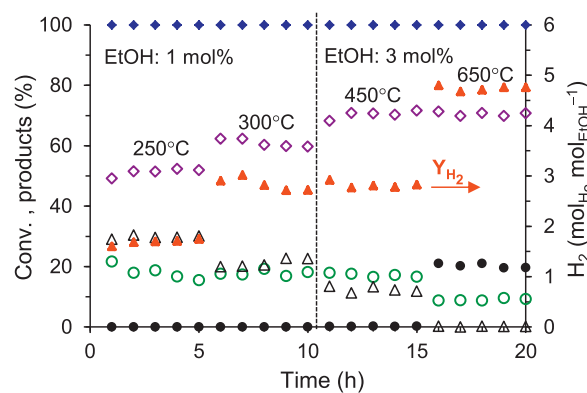

Fig. 2. Conversion of ethanol (♦), gas-phase products distribution: H_2 (◇), CO_2 (○), CO (●), CH_4 (△), and H_2 yield (▲) on the $Ni_{12}Mg_2AlO_Y$ catalyst. The reaction is stopped and started again when changing ethanol concentration.

No CO or acetaldehyde is obtained. Methane transformation is logically more pronounced at 300 °C (compared to 250 °C); as a result, a higher proportion of H_2 is obtained. However, it is necessary to remark that, as the conversion is total, a part of the catalyst can be enough to totally convert ethanol and the other part can transform the products. The H_2 yield reaches 3 mol mol_{EtOH}^{-1} at 300 °C, which can correspond to 100% of H_2 yield in total decomposition of ethanol to hydrogen. The present catalyst remains stable after at least 10 h of the reaction while a carbon formation is obtained and reported later on.

As expected, higher temperature can lead to higher H_2 yield. As seen in Fig. 2, the $Ni_{12}Mg_2AlO_Y$ catalyst allows obtaining a H_2 production of 4.8 mol mol_{EtOH}^{-1} at 650 °C even in the presence of higher ethanol concentration (EtOH/H_2O/N_2 = 3/9/88) within such a case a carbon formation that increases up to 19 mg. This value is one of the best ever reported for the low-cost catalysts. That is mainly due to the complete methane transformation and relatively lower CO selectivity in our case. It is important to mention that working at high-temperature WGS equilibrium does not allow reaching the theoretical value of 6 mol mol_{EtOH}^{-1}. Our value at 650 °C is comparable to those recently reported for Ni-based catalysts, taking into account the reaction conditions; even if H_2 yields of 5 mol mol_{EtOH}^{-1} ($Ni_{50}ZnAl$ catalyst, H_2O/EtOH = 6) [39] and 5.1 mol mol_{EtOH}^{-1} (Ni/Mg_2Al catalyst, H_2O/EtOH = 8.4) [41] were reported. Compared to other inexpensive catalysts recently reported, such as Co- and Cu-based mixed oxides [42,43], our present results are also competitive. The present $Ni_XMg_2AlO_Y$ catalysts behave stable for ESR. It has been reported previously that the $Ni_3Mg_2AlO_Y$ catalyst also presents a good stability during 10 h at 450 and 650 °C [37]. The stability of the catalyst has been more deeply analyzed on the $Ni_3Mg_2AlO_Y$ compound. As reported in Fig. 3, the $Ni_3Mg_2AlO_Y$ catalyst shows a good stability after 125 h of reaction at 300 °C without any sign of deactivation even if carbon species are formed. Using a noble metal-based catalyst (CeZrCoRh), it has been already previously reported for H_2 production from ESR that total ethanol conversion and stable products distribution can be obtained accompanied with carbonaceous deposits. The conversion decreased to 70% only after 281 h [44]. However, in this case, a higher quantity of catalyst has been used (0.16 g) for the stability tests.

The $Ni_XMg_2AlO_Y$ catalysts are able to completely convert ethanol and produce the expected products of ESR at 300 °C, i.e. H_2 and CO_2 with the addition of CH_4. The average H_2 yield is obtained at 3 mol mol_{EtOH}^{-1}. As it is known that increasing water–ethanol ratio allows obtaining higher H_2 yield [39], hence the performance obtained here with a H_2O/EtOH ratio of 3 is very high as compared to the literature. Even if very recently it has been
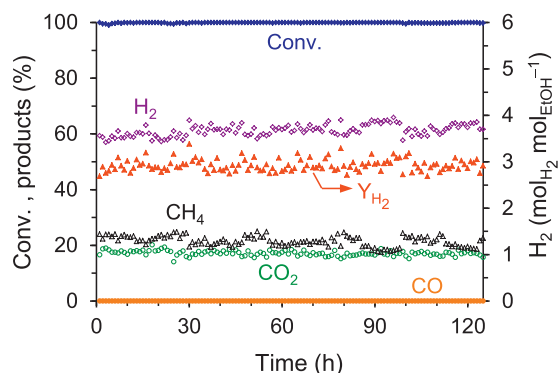
Fig. 3. Conversion of ethanol (♦), gas-phase products distribution: H_2 (◇), CO_2 (○), CO (●), CH_4 (△), and H_2 yield (▲) at 300 °C on the $Ni_3Mg_2AlO_Y$ catalyst as a function of time on stream. $EtOH/H_2O/N_2 = 1/3/96$.

reported that $Rh–Co/CeO_2$ catalyst can lead to a CO-free H_2 yield of 4.3 mol mol_{EtOH}^{-1} at 300 °C, the value was obtained using a very high $H_2O/EtOH$ ratio at 10 [18]. Furthermore, the value corresponded to an initial state obtained after only 25 min, afterwards the catalyst deactivated. In a recent study, $Rh–Fe/Ca–Al_2O_3$ catalyst was developed as efficient and stable catalyst for ESR at low temperature. A H_2 yield of 3.5 mol mol_{EtOH}^{-1} was reported at 300 °C but using a large amount of water ($EtOH/H_2O/N_2 = 1/10/89$) [17]. Moreover, CO was formed in the gas-phase products at 300 °C but could be suppressed at 350 °C. It seems that the present catalysts allow totally transforming CO at low temperature of 300 °C through WGS to H_2 and probably disproportionation to carbon, as 134 mg of carbon is measured after the experiment of 125 h.

To be able to report high conversion at low temperature, low concentration of ethanol is favorable. Fig. 4 compares the influence of ethanol concentration for ESR on the $Ni_{12}Mg_2AlO_Y$ catalyst at 250 °C. With a low ethanol concentration (1 mol.%), total ethanol conversion and the expected products of ESR are obtained. While with a higher ethanol concentration (3 mol.%), conversion decreases to about 60% and the gas-phase products obtained are almost exclusively H_2 (70%) and acetaldehyde (28%) with a small
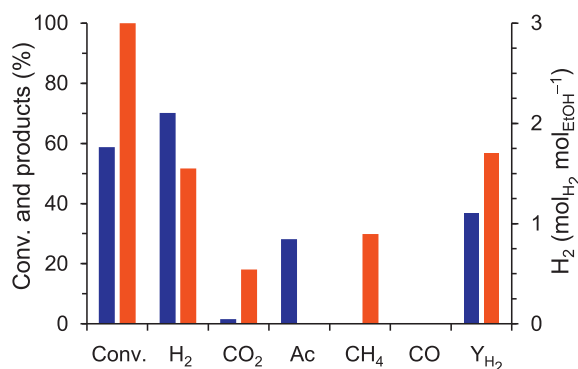

Fig. 4. Conversion of ethanol, gas-phase products distribution, and H_2 yield (Y_{H2}) at 250 °C on the $Ni_{12}Mg_2AlO_Y$ catalyst. $EtOH/H_2O/N_2 = 3/9/88$ (blue), $EtOH/H_2O/N_2 = 1/3/96$ (red). Ac: acetaldehyde.

amount of CO_2 (2%), which demonstrates that dehydrogenation of ethanol is the dominant reaction in such conditions.

Finally, the $Ni_XMg_2AlO_Y$ catalysts are very active at low temperature as shown by the high H_2 yield obtained and they are able to sustain harsh conditions as presented before. The catalytic activity remains stable even under higher concentration of the reactant mixture. However, it is shown that working with higher concentration of ethanol at low temperature leads to lower conversion and different products distributions.

3.2. Production of nanofibrous carbon

Carbon formation obtained under the different catalytic conditions previously reported is summarized in Table 1. At low temperature up to 250 °C, no carbon is formed, with very low ethanol concentration (1 mol.%) even with the highest Ni content studied. When temperature increases to 650 °C, carbon formation depends on Ni content and ethanol concentration. When ethanol concentration is increased to 14 mol.%, carbon formation at 450 °C is largely increased to 0.12 g g^{-1} h^{-1} for $Ni_3Mg_2AlO_Y$ and 0.40 g g^{-1} h^{-1} for $Ni_{12}Mg_2AlO_Y$. In such a case, Ni content clearly influences the carbon formation rate. In fact, it was reported for carbon materials from ethanol decomposition that a high amount of carbonaceous reactant (50 vol.% of ethanol) was required to obtain high yield of solid carbon, and high Ni content (≥ 80 mol.%) also promoted co-generation of H_2 and carbon [32,34].

Hence we show very promising results that H_2 and carbon nanofibrous materials can be produced at the same time on well dispersed highly loaded $Ni_XMg_2AlO_Y$ catalysts at low temperature from ethanol in the presence of water, while it has been reported that this is possible only at high temperature [34]. The carbon nanomaterials formation such as carbon nanotubes and/or carbon nanofibers can be seen as an added bonus. Carbon formation obtained in the present study is probably related at low temperature to the tranformation of CO on metallic nickel. Red'kin and Kipin [40] showed that during the pyrolysis on a nickel catalyst (in the absence of water), the ethanol molecule led to a sequence of chemical transformation, eventually decomposing into H_2, CH_4, and CO. While at high temperature carbon can be obtained from methane. It was proposed that methane dehydrogenation and Boudouard reaction [Eq. (9)] were the two probable routes for the generation of filamentous carbon during ESR between 400 and 700 °C [45,46]. Xu et al. further pointed out that a water-rich atmosphere like ethanol in the presence of water favored the formation of carbon filaments [45]. We also found that H_2 production as well as filamentous carbon was obtained on the Ni-based catalysts by ESR probably through the decomposition of ethanol [36,37].

It is generally accepted that carbon growth takes place on the nickel particle [47]. Carbon nanofibers of various thicknesses or carbon nanotubes could be obtained by varying the process conditions, and diameter of filamentous carbon was related to the metal particle size [47]. Catalytic decomposition of ethanol (i.e. in the absence of water) was also used to grow nano-sized carbon filaments on polycrystalline nickel foam [48]. Moreover, as carbon nanofilaments are observed in the present study, it can be proposed that ethanol can also be decomposed in the presence of water. It can

Table 1
Production of carbon reported in g g^{-1} h^{-1} on the $Ni_XMg_2AlO_Y$ catalysts.

Catalyst	1 mol.% EtOH $T = 250$ °C	1 mol.% EtOH $T = 300$ °C	3 mol.% EtOH $T = 650$ °C	14 mol.% EtOH $T = 450$ °C
$Ni_3Mg_2AlO_Y$	n.d.	0.02[a]	0.02[b]	0.12[c]
$Ni_{12}Mg_2AlO_Y$	0[b]	0.02[b]	0.04[b]	0.40[c]

[a] Measured after 125 h.
[b] Measured after 10 h.
[c] Measured after 30 h.

Table 2
Compositions, specific surface areas, and crystalline parameters of the $Ni_XMg_2AlO_Y$ catalysts.

Catalyst	Ni loading (wt%)[a]	Ni/Mg/Al ratio[b]	Ni/M_T[b]	S_{BET} (m² g⁻¹)	d (nm)[c]	Lattice (nm)[d]
$Ni_3Mg_2AlO_Y$	43.7	3/2/1	0.5	168	3.9	0.38
$Ni_{12}Mg_2AlO_Y$	61.4	12/2/1	0.8	196	5.9	0.26

[a] Measured by ICP-MS.
[b] Deduced from elemental analysis.
[c] Particles size of oxide crystals calculated from (220) plane.
[d] Lattice parameter α.

be therefore expected that varying the experimental conditions will also lead to different filamentous carbon. Carbon nanomaterials are important materials not only in catalysis as support but also for various applications, such as electrochemical capacitors [49] and H_2 storage [50]. Therefore, CNTs and/or CNFs obtained through the present ESR process can potentially bring down the price of carbon nanofibrous materials, showing an alternative way of the low-cost synthesis.

3.3. Characterizations of the $Ni_XMg_2AlO_Y$ catalysts

3.3.1. Elemental analysis and surface area

A series of $Ni_XMg_2AlO_Y$ (0 < X ≤ 4) ex-hydrotalcite catalysts has been recently reported [37]. In the present study, two compounds with high Ni content are analyzed. In particular, the $Ni_{12}Mg_2AlO_Y$ compound presents a high Ni loading of 61.4 wt%. The Ni/Mg/Al molar ratios obtained by ICP-MS spectrometry are almost the same as the nominal values (Table 2), showing the successful co-precipitation without any loss of the components. It was shown that $Ni_XMg_2AlO_Y$ (X ≤ 4) catalysts have relatively large surface areas between 100 and 180 m² g⁻¹ [37]. There is a global increase in the surface area when the Ni content increases and the $Ni_{12}Mg_2AlO_Y$ catalyst presents the maximum value of 196 m² g⁻¹ in the studied series.

3.4. XRD study

3.4.1.1. XRD on the calcined catalysts

The XRD patterns of $Ni_XMg_2AlO_Y$ catalysts with different Ni contents have been studied (Fig. 5A). For $Ni_XMg_2AlO_Y$ catalysts with X ≤ 4, the XRD patterns have been already reported [37], however, the $Ni_3Mg_2AlO_Y$ catalyst is still reported in Fig. 5A for easy comparison. The nanocomposites demonstrate patterns of NiO (47-1049 JCPD file), Ni–Mg–O solid solution (24-0712 JCPDS file) and/or MgO (65-0476 JCPDS file). The diffraction lines of the above phases almost overlap each other. There is no relevant peak to Al_2O_3, which can be due to the high dispersion, amorphous phase of aluminum species, and/or the insertion of aluminum species into Ni–Mg–O phase to form Ni–Mg–Al–O solid solution. A careful examination further reveals the influence of nickel loading. The patterns appear more intense and thinner when the Ni content increases. This is in agreement with the slight growing average particles size of oxide crystal (Table 2). Small oxide nanoparticles between 4 and 6 nm are measured for the $Ni_XMg_2AlO_Y$ catalysts when Ni loading increases. The nanocomposite becomes closer to bulk NiO if the Ni content is very high such as in $Ni_{12}Mg_2AlO_Y$, but Ni–Mg–(Al)–O phase is still expected.

The lattice parameter α of $Ni_XMg_2AlO_Y$ catalysts (X ≤ 4) decreased with Ni content, in agreement with the formation of Ni–Mg–(Al)–O solid solution [37]. The $Ni_{12}Mg_2AlO_Y$ compound presents a smaller value of 0.26 nm (Table 2), following the evolution of the series of catalysts studied. When Ni content increases Mg cations may be substituted by Ni cations. Ni^{2+} radius (0.069 nm) is in fact smaller than that of Mg^{2+} (0.072 nm), which leads to the
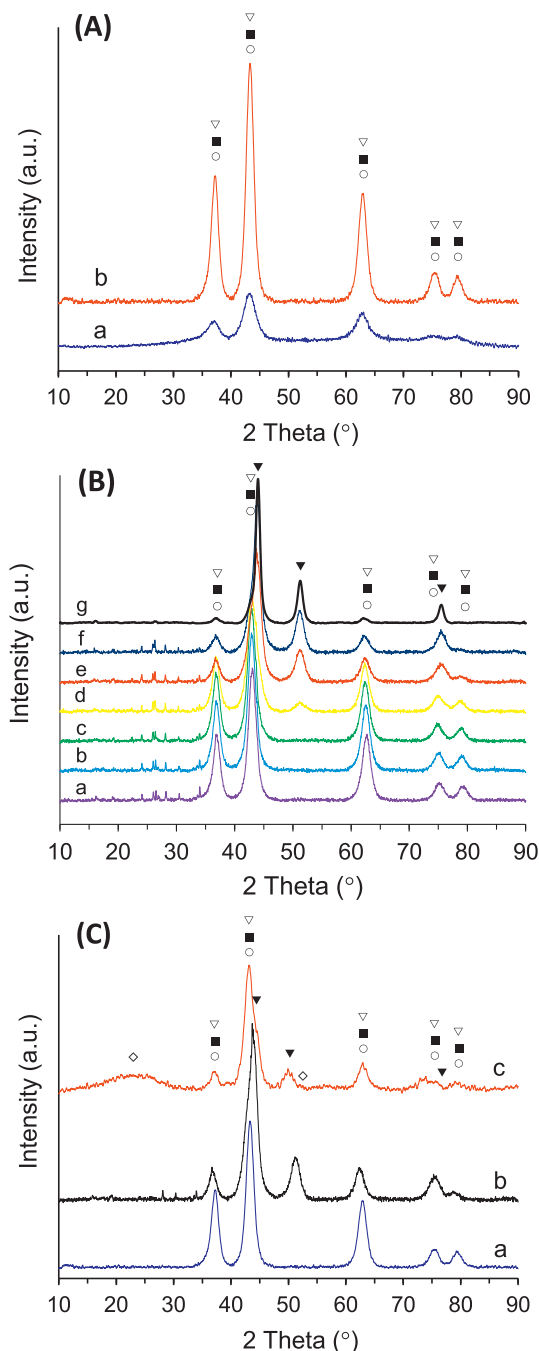

Fig. 5. (A) XRD patterns of the calcined $Ni_XMg_2AlO_Y$ catalysts. X = (a) 3, (b) 12. (B) XRD patterns of the $Ni_{12}Mg_2AlO_Y$ catalyst obtained by in situ reduction in H_2. (a) 30 °C, (b) 164 °C, (c) 365 °C, (d) 450 °C, (e) 450 °C for 10 h, (f) 560 °C, and (g) 650 °C. (C) XRD patterns of the $Ni_{12}Mg_2AlO_Y$ catalyst. (a) Calcined at 500 °C, (b) treated with H_2 at 450 °C for 10 h, (c) after ESR (T = 300 °C, EtOH/H_2O/N_2 = 1/3/96). Peaks assigned to NiO (▽), Ni–Mg–(Al)–O (■), MgO (○), Ni (▼), C (◇).
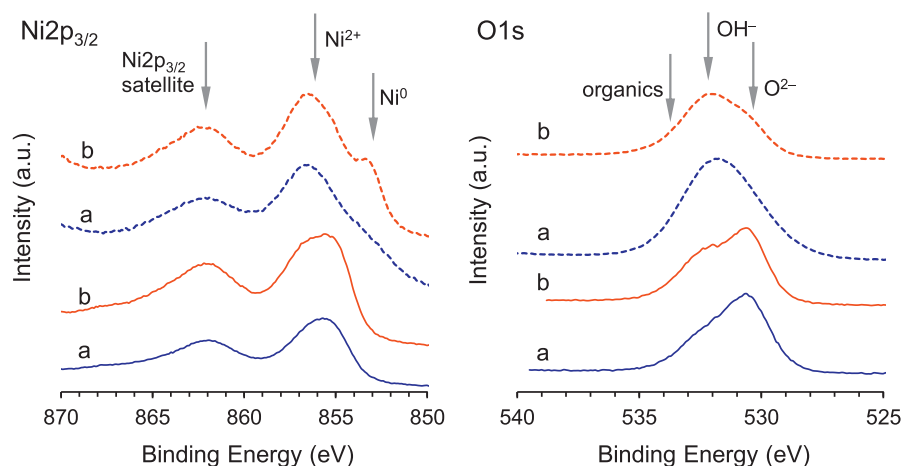
Fig. 6. Ni $2p_{3/2}$ and O 1s XPS spectra of the calcined (solid line) and used (dashed line) $Ni_XMg_2AlO_Y$ catalysts. (a) $X = 3$ ($T = 650\,°C$, $EtOH/H_2O/N_2 = 3/9/88$) from our previous paper [37], (b) $X = 12$ ($T = 300\,°C$, $EtOH/H_2O/N_2 = 1/3/96$).

reduction of the average distance of metal ions within the oxides, as a result, the lattice parameter decreases.

3.4.1.2. In situ XRD in H_2 on the $Ni_{12}Mg_2AlO_Y$ catalyst

Fig. 5B shows the XRD patterns of the $Ni_{12}Mg_2AlO_Y$ catalyst obtained from the in situ reduction with H_2. All the diffraction peaks of NiO, Ni–Mg–(Al)–O solid solution, and/or MgO are maintained in the temperatures range analyzed (30–650 °C). The peaks of oxides become less intense when reduction temperature is at 450 °C for 10 h. This treatment condition allows obtaining a partially reduced solid, with the simultaneous generation of anionic vacancies [37], in agreement with TPR results. The particle sizes of oxide crystal show almost no variation depending on the treatment temperature. The values are nearly the same as those of the calcined catalysts (Table 3). Metallic nickel (70-1849 JCPDS file) is visible when temperature is equal or higher than 450 °C. The size of Ni^0 nanoparticles is found at about 4.9 nm at 450 °C, and then it slightly grows up to 6 nm at 650 °C.

3.4.1.3. XRD on the used $Ni_{12}Mg_2AlO_Y$ catalyst

The $Ni_{12}Mg_2AlO_Y$ catalyst after ESR as shown in Fig. 5C presents similar patterns to those obtained on the catalyst before reaction (after treatment in H_2). All the oxide phases still remain, as well as metallic Ni^0 phase. The particles sizes of NiO, Ni–Mg–(Al)–O, and/or MgO after ESR are measured at 4.2 nm for the $Ni_3Mg_2AlO_Y$ catalyst and at 5.4 nm for the $Ni_{12}Mg_2AlO_Y$ catalyst (Table 3). The values are very close to those measured for the calcined $Ni_XMg_2AlO_Y$ nanocomposites. The values are also found nearly the same as the one obtained in H_2 treatment (in situ XRD). The Ni^0 particles sizes are measured at 4.5 nm for $Ni_3Mg_2AlO_Y$ and at 5.0 nm for $Ni_{12}Mg_2AlO_Y$ after ESR. The data are very similar to those obtained during in situ treatment in H_2. The size distribution of nickel-related particles estimated from TEM is also reported in Fig. 11A and C. An average particle size of 4.5 nm is estimated for the $Ni_3Mg_2AlO_Y$ catalyst, while a size of 6.0 nm is estimated for the $Ni_{12}Mg_2AlO_Y$ catalyst. Therefore, there is no aggregation of nickel species observed for the present $Ni_XMg_2AlO_Y$ catalysts after ESR. All the Ni-related particles are shown in uniform and small sizes even under the reactant mixtures. The oxide crystal exhibits stability during the reaction because of the presence of strong interactions between Ni^{2+} cations and Mg^{2+} or/and Al^{3+} cations probably due to the incorporation of nickel species into Mg–(Al)–O phase. This enables to lead to a very stable active center with enhanced interactions.

Table 3
Particle sizes of the $Ni_XMg_2AlO_Y$ catalysts obtained in different conditions from XRD and TEM.

Conditions	$Ni_3Mg_2AlO_Y$		$Ni_{12}Mg_2AlO_Y$	
	d oxide crystals (nm)	d Ni^0 (nm)	d oxide crystals (nm)	d Ni^0 (nm)
Calcined at 500 °C	3.9	n.d.	5.9	n.d.
Treated in H_2[a]	4.0	4.0	5.5	5.0
Used	4.2[b]	4.5[b]	5.4[c]	5.0[c]
	4.5[b,d]	4.5[b,d]	6.0[c,d]	6.0[c,d]

[a] At 450 °C for 10 h.
[b] After 5 h of reaction at 450 °C, $EtOH/H_2O/N_2 = 14/42/44$.
[c] After 5 h of reaction at 300 °C, $EtOH/H_2O/N_2 = 1/3/96$.
[d] Nickel-related particles size estimated from TEM.

Table 4
XPS parameters of the $Ni_XMg_2AlO_Y$ catalysts obtained in different conditions.

Conditions	$Ni_3Mg_2AlO_Y$[a]		$Ni_{12}Mg_2AlO_Y$[a]	
	Ni $2p_{3/2}$ (eV)	O 1s (eV)	Ni $2p_{3/2}$ (eV)	O 1s (eV)
Calcined at 500 °C	855.7 (3.6)	530.6/531.7 (3.1)	856.0 (4.1)	530.6/531.7 (3.4)
Used after ESR	856.5 (5.1)[b]	532.2 (3.7)[b]	856.5 (5.5)[c]	532.4 (3.8)[c]

[a] Full-width at half-maximum (FWHM) values are reported in parentheses.
[b] After 5 h of reaction at 450 °C, $EtOH/H_2O/N_2 = 14/42/44$.
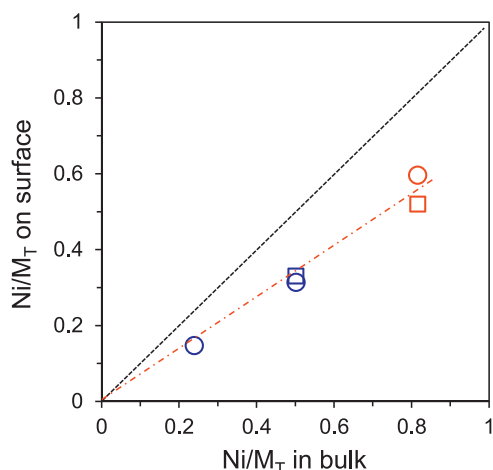[c] After 5 h of reaction at 300 °C, $EtOH/H_2O/N_2 = 1/3/96$.

Fig. 7. Variation of surface Ni/M_T ratio as a function of bulk Ni/M_T ratio. (○) The calcined $Ni_XMg_2AlO_Y$ catalysts, (□) the used $Ni_XMg_2AlO_Y$ catalysts. Our previous results are also present in blue for comparison [37].

As the carbon formed has been manually separated from the catalyst, some carbon remains on the catalyst. The XRD patterns of the used $Ni_{12}Mg_2AlO_Y$ catalyst after ESR at 300 °C in diluted conditions (EtOH/H_2O/N_2 = 1/3/96) (Fig. 5C, c) could reveal the presence of CNTs as evidenced by the characteristic reflection at $2\theta = 53°$ for (004) plane according to 58-1638 JCPDS file, however, it is not clearly seen due to the overlapping by the Ni^0 phase. The broad peak visible at $2\theta = 26°$ was generally attributed to the graphitic carbon in the literature [51,52].

3.4.2. XPS study
3.4.2.1. XPS on the calcined catalysts

Ni 2p core-level spectra are reported in Fig. 6, and the related binding energies are summarized in Table 4. A main emission peak in Ni $2p_{3/2}$ region is observed. The $Ni_3Mg_2AlO_Y$ and $Ni_{12}Mg_2AlO_Y$ catalysts show almost the same BE at about 855.7 eV that is close to 855.5 eV reported for the Ni–Mg–Al mixed oxides [53]. The BEs are found higher than those reported for bulk NiO in the literature [54,55], but close to that observed for $NiAl_2O_4$ (856 eV) [56]. This demonstrates the strong interactions between Ni^{2+} species with Mg^{2+} and/or Al^{3+} cations due to the different electron transfer effects. In fact, $Ni_1Mg_2AlO_Y$ showed a higher BE at 856.1 eV [37]. In addition, the Ni $2p_{3/2}$ satellites are visible up to the main peak. This satellite line has been interpreted by a predominant surface plasmon loss due to a two hole $c3d^94s^2$ final state effect as the characteristic presence of Ni^{2+} species [57]. Moreover the Ni $2p_{3/2}$ band shape exhibits a line broadening effect when the Ni content increases (Table 4), indicating the possible co-presence of different Ni^{2+} species that interact with other metal cations.

As reported in Fig. 6, O 1s core-level shows two peaks at BEs of 531.7 and 530.6 eV for the $Ni_3Mg_2AlO_Y$ and $Ni_{12}Mg_2AlO_Y$ catalysts, respectively. The peak at 531.7 eV has been found in the catalyst precursors, which is assigned to the oxygen species in OH$^-$ groups [55,57]. The peak at 530.6 eV can be attributed to the typical O^{2-} lattice oxygen species in oxides of NiO, Ni–Mg–(Al)–O solid solution, and/or MgO [53,54]. To be recalled, only one peak at 531.7 eV was observed for the $Ni_1Mg_2AlO_Y$ catalyst with low Ni content. This agrees with the broadening effect of O 1s line when Ni content increases (Table 4).

Some quantitative XPS features allow obtaining additional information. Fig. 7 compares the surface Ni molar ratio determined by XPS to the bulk Ni molar ratio measured by ICP-MS, where the variation of Ni concentration between surface and bulk may be observed. The 45° diagonal line corresponds to the ideal case of

the homogeneous distribution of nickel inside the solids. It can be seen that the Ni/M_T ratio on surface appears relatively lower than that in bulk in the $Ni_XMg_2AlO_Y$ catalysts, probably due to some segregation on the calcined compounds. The obtained relatively linear relationship demonstrates the homogeneous distribution of nickel species inside the present studied $Ni_XMg_2AlO_Y$ catalysts even up to a high Ni content of about 60 wt%. The XPS results reach very good agreement with the XRD analysis. Small and relatively uniform nanoparticles of NiO and/or Ni–Mg–(Al)–O are analyzed by XRD. All the above results show the presence of Ni^{2+} cations on the surface of the $Ni_XMg_2AlO_Y$ catalysts, with strong interactions with other cations that are well maintained even with a high Ni content.

3.4.2.2. XPS on the used catalysts

The used $Ni_XMg_2AlO_Y$ catalysts show a BE at 856.5 eV for Ni $2p_{3/2}$ (Fig. 6, Table 4). The value is higher compared to the calcined catalysts (Table 4), but it becomes close to the one obtained for Ni^{2+} cations in $Ni(OH)_2$ (856.2 eV) which has been observed for the catalyst precursors. This can be explained by the presence of OH$^-$ groups at the surface of the used catalysts under the mixture of ethanol and water. The characteristic satellite line due to Ni^{2+} species is clearly visible. Ni^0 species that are observed on the $Ni_{12}Mg_2AlO_Y$ catalyst may possibly also co-exist with Ni^{2+} cations after ESR on the $Ni_3Mg_2AlO_Y$ catalyst, in agreement with observation of a broadening effect. However, Ni^{2+} cations are clearly dominant over Ni^0 species whatever the compound. The surface Ni/M_T ratios after ESR are found very close to the values obtained on the calcined catalysts (Fig. 7), showing the good maintenance of the homogeneous distribution of nickel species in the catalysts even after the reaction.

O 1s presents only one broader peak (Fig. 6) compared with two peaks observed on the calcined catalysts. Both the higher BE (532.3 ± 0.1 eV) and the broadening effects disclose the presence of different oxygen species (Table 4). It is highly probably due to the oxygen species in OH$^-$ groups and the oxygen species in the surface-absorbed organic functional groups. It was reported that O 1s line between 531.9 and 533.1 eV is the contribution of different O-containing organic functional groups [58]. Moreover, the surface O/Ni molar ratio after ESR in the present work is much higher than 2, showing the co-presence of different oxygen species on the surface of the used catalysts. All the XPS results (before and after test) are in good agreement with XRD, showing the presence of a robust center composed of Ni^{2+} cations and other cations.

3.4.3. H₂-TPR study

In the literature, Ni–Mg–Al ex-hydrotalcite compounds basically presented a broad peak in TPR analysis at high temperatures between 750 and 850 °C, which was interpreted by the strong incorporation of nickel into Mg–Al support to form Ni–Mg–O and/or Ni–Mg–Al–O solid solutions [46,52]. We reported that $Ni_XMg_2AlO_Y$ catalysts ($0.5 \leq X \leq 4$) showed a main broad TPR peak between 593 and 844 °C. The peak shifted to lower temperature when Ni content increased, because the interactions between nickel species and other cations can be significantly modified by the addition of nickel [37]. To be remarked, to the best of our knowledge, there is no report on the TPR analysis of Ni–Mg–Al–O mixed oxides with very high Ni loading like $Ni_{12}Mg_2AlO_Y$. In the coherence of what has been observed previously, the $Ni_{12}Mg_2AlO_Y$ catalyst shows a TPR peak at lower temperature of 560 °C (Fig. 8). For low Ni content, the strong interactions between nickel species and Al^{3+} and/or Mg^{2+} cations either in the Ni–Mg–(Al)–O solid solution and/or at the interface of nanoparticles of NiO and/or Ni–Mg–(Al)–O make the solid difficult to reduce. While if the Ni content increases, the reducibility of the compound becomes closer to that of bulk NiO. However, high interactions still exist in $Ni_{12}Mg_2AlO_Y$, because the temperature required for reducing the nickel species is still much higher
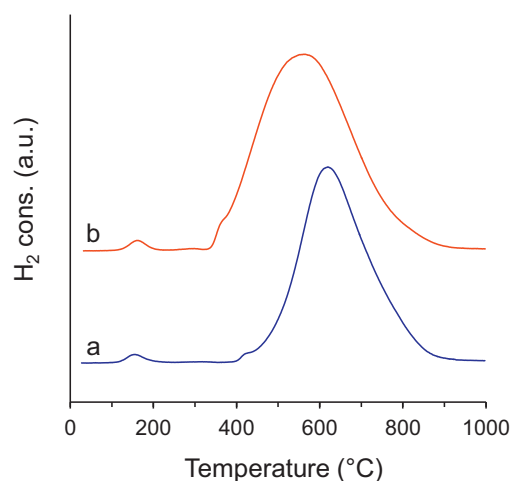
Fig. 8. TPR profiles of the $Ni_XMg_2AlO_Y$ catalysts. X = (a) 3, (b) 12.

Fig. 10. Raman spectra of the carbon species formed on $Ni_{12}Mg_2AlO_Y$ catalyst in the conditions of (a) T = 450 °C, EtOH/H_2O/N_2 = 14/42/44, (b) T = 300 °C, EtOH/H_2O/N_2 = 1/3/96.

than the one needed to reduce bulk NiO (ca. 390 °C) reported in the literature [41,52].

It was previously disclosed that H_2 is quantitatively consumed in proportion to Ni content of the $Ni_XMg_2AlO_Y$ catalysts. A linear relationship can be built between the total H_2 consumption during TPR and the Ni content of the solids [37]. We find that $Ni_{12}Mg_2AlO_Y$ catalyst also well fits to the curve. The H/Ni atomic ratio obtained for $Ni_{12}Mg_2AlO_Y$ is of 2.4, which is in agreement with the values reported for $Ni_XMg_2AlO_Y$ compounds ($X \leq 4$). The H/Ni ratios are higher than the stoichiometric value of 2 that is necessary to reduce quantitatively NiO into Ni^0 according to [Eq. (11)], which can be attributed to the presence of hydrogen spillover species.

$$Ni^{2+} + O^{2-} + H_2 \rightarrow Ni^0 + H_2O + \square \tag{11}$$

with $\square$ being the anionic vacancy.

3.5. Characterizations of nanofibrous carbon

3.5.1. O_2-TPO study

The carbon species formed on the $Ni_{12}Mg_2AlO_Y$ catalyst are graphitic in nature, which is supported by an intense TPO peak between 500 and 650 °C (Fig. 9). No amorphous carbon is observed that is highly reactive toward O_2 and easily oxidized at temperatures lower than 400 °C [59]. In TPO analysis of carbon materials, the
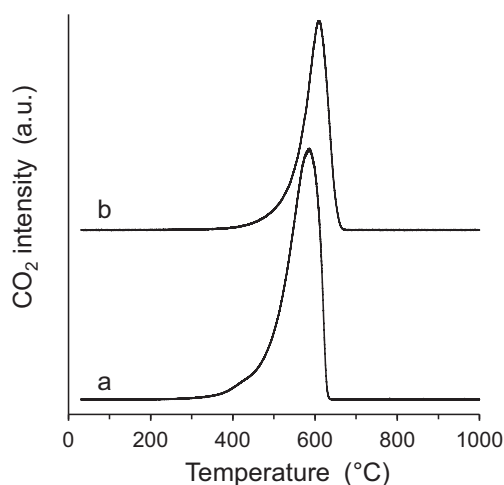

Fig. 9. TPO profiles of the carbon species formed on the $Ni_{12}Mg_2AlO_Y$ catalyst in the conditions of (a) T = 450 °C, EtOH/H_2O/N_2 = 14/42/44, (b) T = 300 °C, EtOH/H_2O/N_2 = 1/3/96.

peak at approximately 610 °C was attributed to the multi-walled carbon nanotubes (MWCNTs) [60]. In a recent study of glycerol steam reforming over Ni–Mg–Al catalyst, the TPO peak of carbon at about 650 °C was also assigned to high-quality MWCNTs [35]. The peak at about 510 °C was ascribed to the single-walled nanotubes (SWCNTs), however, carbon nanofibers (CNFs) were also reported to demonstrate a TPO peak at around 500 °C [60].

Therefore, the present TPO peaks at about 600 °C (605 °C after SRE at 300 °C, in diluted conditions) with relative asymmetry is generally assigned to the graphitic filamentous carbon that can be a mixture of MWCNTs possibly with some CNFs. Compared with our previous results obtained on $Ni_XMg_2AlO_Y$ ($X \leq 4$) catalysts in concentrated conditions (14 mol.% of ethanol) [37], the present TPO peak shifts to higher temperature and becomes thinner and more symmetric when diluted conditions (1 mol.% of ethanol) are used. This suggests that there may be probably higher proportion of CNTs in the carbon species formed.

3.5.2. Raman study

Raman spectroscopy shows two main peaks for the carbon species formed on the $Ni_{12}Mg_2AlO_Y$ catalyst (Fig. 10). The D-band observed at 1349 cm^{-1} is assigned to the vibration of sp^3-hybridized carbon atom in the disordered carbonaceous species, whereas the G-band visible at 1592 cm^{-1} is ascribed to the stretching mode of sp^2-hybridized carbon atom in the ordered graphite [21,36]. Liu et al. [61] reported that CNFs and CNTs can be distinguished by comparing the frequency shift. However, one can tell very slight differences. The carbon species formed on the $Ni_{12}Mg_2AlO_Y$ catalyst is globally attributed to the nanofibrous carbon materials, which is in agreement with the TPO results. It has to be mentioned that the carbon species characterized in the present study are without any acidic treatment or purification.

The intensity ratio of G-band to D-band corresponds to the degree of graphitization. Hence I_G/I_D is characteristic of the degree of the ordered carbon materials. In the literature, the same type of spectra was observed for MWCNTs formed on Ni/Al_2O_3 or Fe/Al_2O_3 catalysts from ethanol decomposition, and the I_G/I_D ratio was measured between 0.9 and 1.5 [31,32]. Similar value of 1.1 is obtained here but in ESR conditions, i.e. in the presence of water and at low temperature. Our result is also comparable to the value reported for CNTs (I_G/I_D = 1.25) formed from glycerol steam reforming at 700 °C over the Ni–Mg–Al catalyst [35]. A higher I_G/I_D ratio is obtained here by using diluted reactant mixture (1 mol.% of ethanol) compared to the data reported in concentrated conditions [37]. This is also in agreement with the observation in TPO analysis.
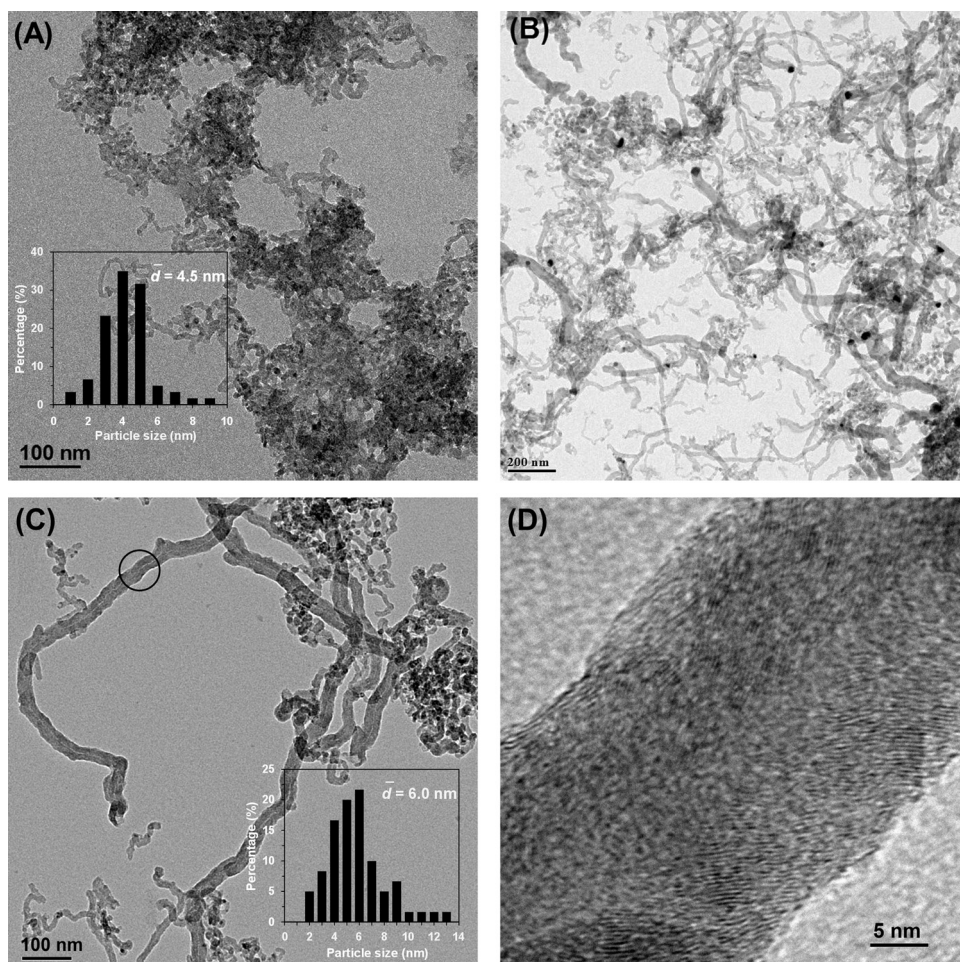
Fig. 11. TEM images of carbon species formed on $Ni_XMg_2AlO_Y$ catalysts. (A) $X = 3$ ($T = 450\,°C$, $EtOH/H_2O/N_2 = 14/42/44$), (B) $X = 12$ ($T = 450\,°C$, $EtOH/H_2O/N_2 = 14/42/44$). (C) $X = 12$ ($T = 300\,°C$, $EtOH/H_2O/N_2 = 1/3/96$), (D) a magnification of the selected area in image (C).

3.5.3. TEM study

One can clearly see the nanofibrous carbon grown on the $Ni_XMg_2AlO_Y$ catalysts in different conditions (Fig. 11A–C). Most of the carbon filaments obtained in diluted conditions are tubular MWCNTs, which are composed of graphitic sheets as shown in Fig. 11D. This observation further confirms the results of TPO and Raman. The lengths are roughly estimated up to tens of micrometer and the diameters are measured at 10–30 nm. The graphitic sheets are found not parallel to the tube axis, but appear to be a fish-bone type in the cross-section. In the literature, the similar structure has been reported for MWCNTs by several research groups [33,52]. To be noted, Ni-related particles are observed at the tip of the carbon filaments, showing nickel species may be accessible. It was proposed that the formation of amorphous carbon on the catalyst may encapsulate the active particles and prevent ethanol from reaching the catalyst or poison the active sites [32].

3.6. Active site and mechanism proposition

Ni-based ex-hydrotalcite catalysts have been recently reported as good candidates for ESR [38,39,41,46,52]. The good catalytic activity, selectivity, and stability were mainly illustrated by the strong interactions between nickel species and other cations, no matter in ternary Ni–M–Al (M = Mg, Zn) systems [39,41,52] or in Cu- and Zn-promoted Ni–Mg–Al quaternary systems [38,46]. More recently, Li et al. [62] reported a nanocomposite $Ni@ZrO_2$ catalyst with enhanced metal–support interaction could prevent metal particles from aggregation, leading to a good stability. The present $Ni_XMg_2AlO_Y$ nanocomposites with high Ni loading are composed of small and uniform nanoparticles of NiO, Ni–Mg–(Al)–O, and/or MgO with relatively large surface areas. Ni^{2+} species are found well distributed in both surface and bulk states whatever before or after the reaction. It is shown that strong interactions exist between Ni^{2+} cations and other cations. The treatment in H_2 at 450 °C leads to partially reduced composites with simultaneous generation of anionic vacancies. The active nickel species existing as Ni^{2+} and/or $Ni^{\delta+}$ in the system interact closely with other cations (Mg^{2+} and/or Al^{3+}) either in the Ni–Mg–(Al)–O solid solution and/or at the interface among nanoparticles of NiO, Ni–Mg–(Al)–O, and/or MgO. It was proposed in a recent paper that Co^{2+} cations are the active site for ESR over Co–Mg–Al ex-hydrotalcites [63]. Moreover, it was already reported that anionic vacancies can be created in Mg–Al compound leading to the presence of coordinately unsaturated cations [64,65]. When nickel is added into the binary Mg–Al compound, the number of anionic vacancies can certainly increase. We previously observed nearly a constant activity of $Ni_XMg_2AlO_Y$ ($X \leq 4$) catalysts reported in mole of ethanol converted per mole of nickel per hour [37]. This suggests that the number of active sites well respect to the Ni loading. Moreover the same activity in mole per mole of Ni per hour is obtained here over the $Ni_XMg_2AlO_Y$ catalysts compared to the activity previously obtained over low Ni loaded $Ni_{0.5}Mg_2AlO_Y$ catalyst [37], as shown in Fig. 12. Therefore, the same Ni species are also obtained with higher Ni content in $Ni_XMg_2AlO_Y$ catalysts, even if the Ni content has been largely increased in the present study.
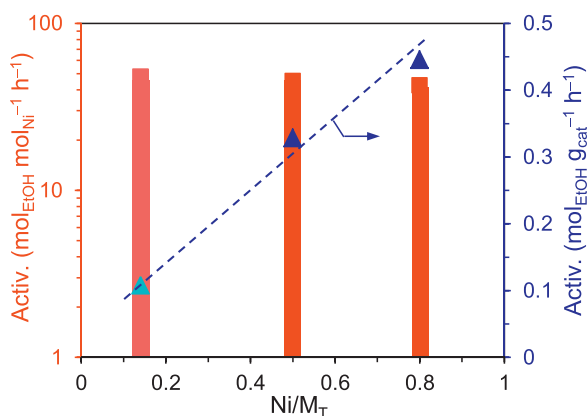
Fig. 12. Activity at 450 °C for ESR (14% of EtOH) of the $Ni_XMg_2AlO_Y$ catalysts pretreated in H_2 at 450 °C versus Ni content. (The result obtained on $Ni_{0.5}Mg_2AlO_Y$ catalyst ($Ni/M_T = 0.14$) from ref [37] is added for comparison).

Thus more active sites with the same activity can be generated in the catalyst with the growing of Ni loading. Ni^0 can also participate but cannot explain all the results obtained.

Therefore, the same active site as previously reported for $Ni_XMg_2AlO_Y$ ($X \leq 4$) can be proposed for the highly loaded $Ni_XMg_2AlO_Y$ catalysts (Scheme 1) [37]. It is modeled by an ensemble of two cations in strong interactions together with anionic vacancies and O^{2-} species, noted as $^XNi - {}^YM$ (with X and Y representing the unsaturation degree of each cation). This model also presents the advantage to reach good agreement with the synergetic effect observed when several cations with strong interactions are present in a mixed oxide, which enables also to prevent the sintering of metal particles. Depending on the unsaturation degree different products can be obtained. The anionic vacancies that are created during the activation treatment in H_2 at 450 °C allow for the heterolytic dissociation of H_2 forming H^- and H^+ species. Therefore, the $^XNi - {}^YM$ active site involves also hydrogen species of hydride nature. As demonstrated in Scheme 1, such a $^3Ni - {}^1M$ site leads to the formation of H_2, CH_4, and CO. In fact, as proposed for H_2, one anionic vacancy allows heterolytic dissociation of ethanol and a lower unsaturation degree ($^1Ni - {}^1M$ site), that is certainly obtained at low temperature, explains the production of acetaldehyde and H_2 (Fig. 4) as previously proposed [37]. It can be remarked that when conversion of ethanol is total, one part of the catalyst could also transform the products obtained, and so acetaldehyde can be further transformed. Depending on the reaction temperature, CH_4 and CO can undergo different routes to be eventually transformed to H_2, CO_2, and carbon, which has been interpreted before. Metallic nickel, which concentration increases with the Ni loading, certainly participates in the reaction when it is in situ formed either in the treatment in H_2 and/or during the reaction, in agreement with the

generally accepted carbon growth on the metallic nickel particle [47].
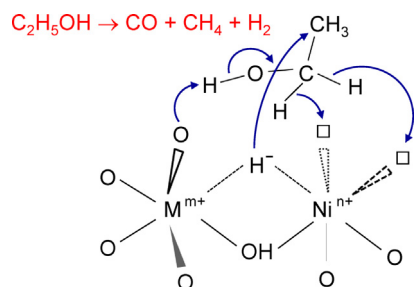
The present $Ni_XMg_2AlO_Y$ catalyst with very high Ni content shows a good catalytic stability after 125 h for ESR with co-generation of nanofibrous carbon. That is mainly because there is no significant structure change of the catalyst under the reaction conditions thanks to the presence of strong interactions between nickel cations and other cations. Such a structure change is believed to gradually deactivate catalyst. On the other hand, the stability is also related to the filamentous carbon formed on the catalyst. As a matter of fact it has been evidenced in several different Ni-based catalytic systems that the formation of filamentous carbon does not deactivate the catalyst for ESR [36,45,46]. While the formation of amorphous carbon or carbonates species lead to the blocking of active sites [44].

4. Conclusion

We report high-yield H_2 production and co-production of carbon nanofibrous materials from ethanol and water at low temperature probably through decomposition of ethanol. The well-dispersed highly loaded noble-metal-free $Ni_XMg_2AlO_Y$ catalysts demonstrate high efficiency toward H_2 production between 250 and 650 °C, accompanied with the co-generation of carbon nano-tubes and carbon nanofibers as added bonus. This can be regarded as a low-cost potential route to produce carbon nanofibrous materials. The influence of ethanol concentration has been analyzed. The $Ni_{12}Mg_2AlO_Y$ catalyst allows total conversion of ethanol at only 250 °C with the production of H_2, CO_2, and CH_4 without formation of carbon, when using a low concentration of ethanol. A CO-free H_2 production of 3 mol mol_{EtOH}^{-1} is obtained at 300 °C with a long life span of 125 h with the generation of graphitic filamentous carbon. For a high concentration of ethanol, total conversion of ethanol is obtained at only 450 °C with the production of H_2, CO_2, CH_4 and a small amount of CO accompanied with the production of graphitic filamentous carbon. The catalysts present advantage to consist of homogeneous and small (4–6 nm) nanoparticles of Ni–Mg–(Al)–O, NiO, and/or MgO. The nickel cations are shown to strongly interact with Mg^{2+} and/or Al^{3+} cations either in the Ni–Mg–(Al)–O solid solution and/or at the interface among nanoparticles of NiO, MgO, and/or Ni–Mg–(Al)–O. An active site is proposed to correspond to the $^XNi - {}^YM$ ensemble (M = Mg^{2+} or Al^{3+}) where the cations are coordinatively unsaturated. Such active sites are active for steam reforming and stable against metal sintering and structure change. We believe that the well-dispersed highly loaded noble-metal-free $Ni_XMg_2AlO_Y$ catalysts will be suitable for other reactions and applications. Moreover, the co-production of clean energy and strategic materials from renewable bioethanol is encouraging and worth performing further studies.

$$C_2H_5OH \rightarrow CO + CH_4 + H_2$$

Scheme 1. Active site modeling and proposition of mechanism for ESR on the $Ni_XMg_2AlO_Y$ catalysts. Ni^{n+}: Ni^{2+} or $Ni^{\delta+}$; M^{m+}: Mg^{2+} or Al^{3+}.

References

[1] A. Midilli, M. Ay, I. Dincer, M.A. Rosen, Renew. Sustain. Energy Rev. 9 (2005) 273–287.
[2] P. Azadi, S. Khan, F. Strobel, F. Azadi, R. Farnood, Appl. Catal. B 117–118 (2012) 330–338.
[3] W. Cai, N. Homs, P. Ramirez de la Piscina, Green Chem. 14 (2012) 1035–1043.
[4] A. Caravaca, A. de Lucas-Consuegra, A.B. Calcerrada, J. Lobato, J.L. Valverde, F. Dorado, Appl. Catal. B 134–135 (2013) 302–309.
[5] A.N. Fatsikostas, D.I. Kondarides, X.E. Verykios, Chem. Commun. (2001) 851–852.
[6] J. Llorca, P.R. de la Piscina, J. Sales, N. Homs, Chem. Commun. (2001) 641–642.
[7] J.P. Breen, R. Burch, H.M. Coleman, Appl. Catal. B 39 (2002) 65–74.
[8] D.K. Liguras, D.I. Kondarides, X.E. Verykios, Appl. Catal. B 43 (2003) 34–354.
[9] A.N. Fatsikostas, X.E. Verykios, J. Catal. (2004) 439–452.
[10] M. Ni, D.Y.C. Leung, M.K.H. Leung, Int. J. Hydrogen Energy 32 (2007) 3238–3247.
[11] P.R. de la Piscina, N. Homs, Chem. Soc. Rev. 37 (2008) 2459–2467.
[12] N. Bion, D. Duprez, F. Epron, ChemSusChem 5 (2012) 76–84.
[13] L.V. Mattos, G. Jacobs, B.H. Davis, F.B. Noronha, Chem. Rev. 112 (2012) 4094–4123.
[14] A.T. Bell, Science 99 (5613) (2003) 1688–1691.
[15] M. Fernández-García, A. Martínez-Arias, J.C. Hanson, J.A. Rodriguez, Chem. Rev. 104 (2004) 4063–4104.
[16] P. Ciambelli, V. Palma, A. Ruggiero, Appl. Catal. B 96 (2010) 18–27.
[17] L. Chen, C.K.S. Choong, Z. Zhong, L. Huang, T.P. Ang, L. Hong, J. Lin, J. Catal. 276 (2010) 197–200.
[18] L. Huang, C. Choong, L. Chen, Z. Wang, Z. Zhong, C. Campos-Cuerva, J. Lin, ChemCatChem 5 (2013) 220–234.
[19] C. Pirez, M. Capron, H. Jobic, F. Dumeignil, L. Jalowiecki-Duhamel, Angew. Chem. Int. Ed. 50 (2011) 10193–10197.
[20] I. Rossetti, C. Biffi, C.L. Bianchi, V. Nichele, M. Signoretto, F. Menegazzo, E. Finocchio, G. Ramis, A. Di Michele, Appl. Catal. B 117–118 (2012) 384–396.
[21] W. Fang, C. Pirez, M. Capron, H. Jobic, F. Dumeignil, L. Jalowiecki-Duhamel, ChemCatChem 5 (2013) 2207–2216.
[22] L. Jalowiecki-Duhamel, C. Pirez, M. Capron, F. Dumeignil, E. Payen, Int. J. Hydrogen Energy 35 (2010) 12741–12750.
[23] L. Jalowiecki-Duhamel, C. Pirez, M. Capron, F. Dumeignil, E. Payen, Catal. Today 157 (2010) 456–461.
[24] Y.J. Wu, P. Li, J.G. Yu, A.F. Cunha, A.E. Rodrigues, Chem. Eng. J 231 (2013) 36–48.
[25] R.H. Baughman, A.A. Zakhidov, W.A. de Heer, Science 297 (2002) 787–792.
[26] P. Hernández-Fernández, M. Montiel, P. Ocón, J.L.G. de la Fuente, S. García-Rodríguez, S. Rojas, J.L.G. Fierro, Appl. Catal. B 99 (2010) 343–352.
[27] A.O. Al-Youbi, J.L. Gómez de la Fuente, F.J. Pérez-Alonso, A.Y. Obaid, J.L.G. Fierro, M.A. Peña, M. Abdel Salam, S. Rojas, Appl. Catal. B 150-151 (2014) 21–29.
[28] Y.-L. Li, I.A. Kinloch, A.H. Windle, Science 304 (2004) 276–278.
[29] D. Sebastián, I. Suelves, E. Pastor, R. Moliner, M.J. Lázaro, Appl. Catal. B 132-133 (2013) 13–21.
[30] J. Gao, J. Zhong, L. Bai, J. Liu, G. Zhao, X. Sun, Sci. Rep. 4 (2014) 3606.
[31] W. Li, H. Wang, Z. Ren, G. Wang, J. Bai, Appl. Catal. B 84 (2008) 433–439.
[32] G. Wang, H. Wang, Z. Tang, W. Li, J. Bai, Appl. Catal. B 88 (2009) 142–151.
[33] D.Z. Mezalira, L.D. Probst, S. Pronier, Y. Batonneau, C. Batiot-Dupeyrat, J. Mol. Catal. A: Chem. 340 (2011) 15–23.
[34] J. Gallego, F. Mondragon, C. Batiot-Dupeyrat, App. Catal. A 450 (2013) 73–79.
[35] C. Wu, Z. Wang, P.T. Williams, J. Huang, Sci. Rep. 3 (2013) 2742.
[36] W. Fang, C. Pirez, M. Capron, S. Paul, T. Raja, P.L. Dhepe, F. Dumeignil, L. Jalowiecki-Duhamel, RSC Adv. 2 (2012) 9626–9634.
[37] W. Fang, S. Paul, M. Capron, F. Dumeignil, L. Jalowiecki-Duhamel, Appl. Catal. B 152–153 (2014) 370–382.
[38] X.-P. Yu, W. Chu, N. Wang, F. Ma, Catal. Lett. 141 (2011) 1228–1236.
[39] C. Resini, T. Montanari, L. Barattini, G. Ramis, G. Busca, S. Presto, P. Riani, R. Marazza, M. Sisani, F. Marmottini, U. Costantino, Appl. Catal. A 355 (2009) 83–93.
[40] A.N. Red'kin, V.A. Kipin, Inorg. Mater. 45 (2009) 982–987.
[41] L.J.I. Coleman, W. Epling, R.R. Hudgins, E. Croiset, Appl. Catal. A 363 (2009) 52–63.
[42] R. Espinal, E. Taboada, E. Molins, R.J. Chimentao, F. Medina, J. Llorca, Appl. Catal. B 127 (2012) 59–67.
[43] B. Lorenzut, T. Montini, L. De Rogatis, P. Canton, A. Benedetti, P. Fornasiero, Appl. Catal. B 101 (2011) 397–408.
[44] M. Araque, J.C. Vargas, Y. Zimmermann, A.-C. Roger, Int. J. Hydrogen Energy 36 (2011) 1491–1502.
[45] W. Xu, Z. Liu, A.C. Johnston-Peck, S.D. Senanayake, G. Zhou, D. Stacchiola, E.A. Stach, J.A. Rodriguez, ACS Catal. 3 (2013) 975–984.
[46] G. Zeng, Q. Liu, R. Gu, L. Zhang, Y. Li, Catal. Today 178 (2011) 206–213.
[47] J. Rostrup-Nielsen, D.L. Trimm, J. Catal. 48 (1977) 155–165.
[48] N. Jeong, J. Lee, J. Catal. 260 (2008) 217–226.
[49] L. Yang, L.R. Hou, Y.W. Zhang, C.Z. Yuan, Mater. Lett. 97 (2013) 97–99.
[50] J.M. Blackman, J.W. Patrick, A. Arenillas, W. Shi, C.E. Snape, Carbon 44 (2006) 1376–1385.
[51] P. Wang, E. Tanabe, K. Ito, J. Jia, H. Morioka, T. Shishido, K. Takehira, Appl. Catal. A 231 (2002) 35–44.
[52] M. Li, X. Wang, S. Li, S. Wang, X. Ma, Int. J. Hydrogen Energy 35 (2010) 6699–6708.
[53] A.F. Lucrédio, J.D.A. Bellido, E.M. Assaf, Appl. Catal. A 388 (2010) 77–85.
[54] A. Ponchel, A. Huysser, C. Lamonier, L. Jalowiecki-Duhamel, Phys. Chem. Chem. Phys. 2 (2000) 303–312.
[55] M.C. Biesinger, B.P. Payne, L.W.M. Lau, A. Gerson, R.S.C. Smart, Surf. Interf. Anal. 41 (2009) 324–332.
[56] S. Velu, K. Suzuki, M. Vijayaraj, S. Barman, C.S. Gopinath, Appl. Catal. B 55 (2005) 287–299.
[57] A.P. Grosvenor, M.C. Biesinger, R.S.C. Smart, N.S. McIntyre, Surf. Sci. 600 (2006) 1771–1779.
[58] B.P. Payne, M.C. Biesinger, N.S. McIntyre, J. Electron. Spectrosc. Relat. Phenom. 185 (2012) 159–166.
[59] S. Natesakhawat, R.B. Watson, X. Wang, U.S. Ozkan, J. Catal. 234 (2005) 496–508.
[60] A.W. Musumeci, G.G. Silva, W.N. Martens, E.R. Waclawik, R.L. Frost, J. Therm. Anal. Calorim. 88 (2007) 885–891.
[61] Y. Liu, C. Pan, J. Wang, J. Mater. Sci. 39 (2004) 1091–1094.
[62] S. Li, C. Zhang, Z. Huang, G. Wu, J. Gong, Chem. Commun. 49 (2013) 4226–4228.
[63] R. Espinal, E. Taboada, E. Molins, R.J. Chimentao, F. Medina, J. Llorca, RSC Adv. 2 (2012) 2946–2956.
[64] J.A. Wang, A. Morales, X. Bokhimi, O. Novaro, T. López, R. Gómez, Chem. Mater. 11 (1999) 308–313.
[65] P.V. Sushko, A.L. Shluger, C.R.A. Catlow, Surf. Sci. 450 (2000) 153–170.